communications biology

A Nature Portfolio journal

Article

https://doi.org/10.1038/s42003-026-10095-1

Integrative single-cell analysis reveals endothelial diversity in the vasa vasorum of human atherosclerosis

Yanzhao Wu[1,2,5], Zhiwei Xue[1,2,5], Tao Sun[1,2,5], Yinda Yu[3], Xiangjun Liang[1,2], Wenchen Xing[1,2], Feiyu Mu[1,2], Zhihan Zhang[1,2], Meilin Lv[1,2], Lu Ling[1,2], Mengtao Han[1,2], Lian Cheng[1,2] ✉, Anton Gisterå[3] ✉ & Donghai Wang[1,2,4] ✉

Microvessels within atherosclerotic plaques are crucially involved in disease progression. Here, we generated a transcriptomic atlas of human atherosclerosis at single-cell resolution, encompassing 17,367 vascular endothelial cells (VECs) from five scRNA-seq studies, and verified key morphological characteristics using histology. *SULF1*$^{+}$ arterial endothelial cells (ArtECs) represented the primary subcluster undergoing endothelial-to-mesenchymal transition (EndMT). Capillary-like endothelial cells (CapECs) were identified as primary mediators of angiogenesis, and a trajectory model illustrated the transition between tip and stalk cells, with subclusters of ArtECs and CapECs predominantly expressing *CXCL12*, thereby driving the CXCL12/CXCR4 signaling axis. The largest plaque EC cluster, exhibiting the most heterogeneity, was found among post-capillary venule endothelial cells (VenECs), particularly *ACKR1*^{high}*NR2F2*^{low} VenECs, which displayed distinct inflammatory transcriptional signatures characterized by adhesion molecules and chemokines. Overall, this atlas of atherosclerosis underscores endothelial heterogeneity and identifies *SULF1*$^{+}$ ArtECs and VenECs as potential therapeutic targets for EndMT and leukocyte recruitment, respectively.

Atherosclerosis is a chronic inflammatory vascular disease characterized by endothelial dysfunction, immune cell infiltration, and lipid accumulation within the arterial wall. Endothelial cells (ECs), which form the inner lining of blood vessels, play a critical role in maintaining vascular homeostasis by regulating blood flow, vascular permeability, and preventing thrombosis[1]. However, under pathological conditions such as oxidative stress, inflammatory stimuli, and disturbed hemodynamics, endothelial cells experience functional impairment, which contributes to the initiation and progression of atherosclerotic lesions[2].

To support vascular function, arteries possess their own microvascular network, known as the vasa vasorum. Under physiological conditions, the vasa vasorum primarily supplies essential nutrients and oxygen to the outer layers of the arterial wall. In large arteries, it also extends to nourish the outer portion of the medial layer, playing a crucial role in maintaining vascular integrity[3]. However, in atherosclerosis, this vascular network undergoes pathological expansion, which is associated with increased neovascularization, inflammatory infiltration, and intraplaque hemorrhage, ultimately contributing to plaque instability[4].

Single-cell sequencing has emerged as a powerful tool to resolve endothelial cell heterogeneity at an unprecedented resolution. While previous studies have identified distinct endothelial cell subclusters, the dynamic functional changes and fate transitions of these subclusters remain poorly understood. Moreover, the interpretation of individual studies may be limited by factors such as small sample sizes, variations in experimental design, and technical biases. Therefore, there remains a need for a standardized single-cell reference, allowing for a deeper understanding of endothelial cell diversity and its role in disease progression.

In this study, we integrated five single-cell studies on human atherosclerosis, employing cASW[5] and iLISI[6] to identify the optimal batch-correction method. Our analysis encompassed both early and advanced lesions, as well as non-lesion samples, ensuring a comprehensive assessment of endothelial cell heterogeneity.

[1]Department of Neurosurgery, Qilu Hospital, Cheeloo College of Medicine and Institute of Brain and Brain-Inspired Science, Shandong University, Jinan, China. [2]Shandong Key Laboratory of Brain Health and Function Remodeling, Jinan, China. [3]Department of Medicine Solna, Center for Molecular Medicine, Karolinska University Hospital, Karolinska Institutet, Stockholm, Sweden. [4]Department of Neurosurgery, Qilu Hospital of Shandong University Dezhou Hospital, Dezhou, China. [5]These authors contributed equally: Yanzhao Wu, Zhiwei Xue, Tao Sun. ✉e-mail: chenglian5667@163.com; anton.gistera@ki.se; drwangdonghai@sdu.edu.cn

Results

Landscape of atherosclerosis endothelial cells at single-cell resolution

To characterize the phenotypic changes in endothelial cells within atherosclerotic plaques, we integrated single-cell transcriptomic data from five independent studies, encompassing 25 patients and 38 samples derived from carotid, coronary and aortic arteries[7–11] (Supplementary Table 1). We retained a total of 200,430 high-quality cells, including 17,762 endothelial cells (ECs). To optimize data integration, we evaluated performance using cASW[5] and iLISI[6], ultimately selecting reciprocal principal component analysis (rPCA)[12] as the most effective strategy (Supplementary Figs. 1A, B, 2A–D, and 3A–G).

Initially, we annotated major endothelial clusters, identifying vascular endothelial cells (VECs) using *PECAM1* and *VWF*, while *LYVE1* and *CCL21* distinguished lymphatic endothelial cells (LECs)[5] (Supplementary Fig. 2D). To further refine classification, we systematically reviewed endothelial cell definition strategies from previous single-cell studies (Table 1). Despite the presence of luminal endothelium in human carotid plaques, immunofluorescence for PECAM1 and ACTA2 revealed numerous small intratissue vascular structures[13], indicating a complex endothelial composition[14] (Fig. 1; Supplementary Table 2). Within the dataset, vascular endothelial cells (VECs) were categorized into three major clusters: arterial endothelial cells (ArtECs), post-capillary venule endothelial cells (VenECs) and capillary-like endothelial cells (CapECs). ArtECs ($n = 4200$) were characterized by high expression of *GJA4*, *GJA5*, and *SEMA3G*. VenECs ($n = 10{,}386$) were defined by *ACKR1* and *NR2F2*[15], while CapECs ($n = 2235$) exhibited enrichment of *RGCC* and *CA4*[16,17] (Fig. 2A, B; Supplementary Data 1). We validated the diverse classification of endothelial cells based on AUCell scoring[18] (Supplementary Fig. 3F). Additionally, we identified two transcriptionally distinct endothelial clusters: a hypoxia-associated cluster, distinguished by high expression of *MT1X*, *MT1E*, and *MT2A*[17,19], and an endothelial-to-mesenchymal transition (EndMT) cluster, marked by elevated expression of *ACTA2* and *MYH11* (Fig. 2A, B; Supplementary Data 1). The presence of VenECs, ArtECs, and CapECs was consistently observed across multiple datasets (Fig. 2C, D), confirming their clustering aligned with expected distribution patterns.

Further refined clustering analysis revealed three VenECs subclusters (E01-E03), three CapECs subclusters (E05-E07), and three ArtECs subclusters (E08-E10), ultimately leading to the identification of 11 distinct endothelial clusters (Fig. 2E, F; Supplementary Fig. 4A, B). Tissue distribution analysis revealed that E03-veins-NR2F2 was consistently detected across datasets. E07-capillaries-IGFBP5 and E08-arteries-CXCL12 remained at stable frequency except in Pan's cohort[10] which contained the fewest VECs (Fig. 2C–E; Supplementary Fig. 4A; Supplementary Data 1). LECs were mainly derived from Hu's cohort[9] (Supplementary Fig. 3G). Among these, *NR2F2*, a key regulator of venous endothelial identity, co-defined VenECs along with *ACKR1*. However, we observed that E03-veins-NR2F2 exhibited high *NR2F2* expression but low *ACKR1* expression (Supplementary Fig. 4B). Comparison with previously reported endothelial markers further underscored the transcriptional diversity among clusters (Supplementary Fig. 4C). E10-arteries-SULF1 exhibited a unique gene expression signature, while *MAFB* was highly expressed in E03-veins-NR2F2. Periostin[20], a secretory extracellular matrix (ECM) protein encoded by *POSTN*, was enriched in VenECs, and IL6 was predominantly expressed in E01-veins-SELE and hypoxia-associated E04 subcluster (Supplementary Fig. 4C). We also explored the relationship between *ACKR1* and *CXCL12* and found no significant positive correlation at the single-cell level (Supplementary Fig. 4D). Regarding endothelial LDL uptake, we found that *CAV1* was more broadly expressed and exhibited higher expression level in ArtECs (Supplementary Fig. 4E). Collectively, these findings provided a refined classification of endothelial heterogeneity within atherosclerotic plaques.

hdWGCNA revealed distinct transcriptional programs among VECs subclusters

High-dimensional weighted gene co-expression network analysis (hdWGCNA) identified three distinct gene co-expression modules and constructed gene interaction networks[21]. Module1 was predominantly enriched in ArtECs and E11-EndMT, whereas Module2 was mainly

Table 1 | Vascular endothelial cell definition strategies in previous single-cell studies

Tissue	VECs resolution	Year	Reference
Carotid and coronary arteries	EC01 (VenECs): *ACKR1*, *STC1*; EC02: *ITLN1*, *BMX*, *SELP*, *DKK2, VWF*	2025	Bleckwehl et al.[63]
Carotid and coronary arteries	EC01 (Classical ECs): *VWF*, *PECAM1*, *ECSCR*; EC02 (EndMT): *VWF*, *PECAM1*, *ECSCR*, *FN1*, *BGN*, *COL8A1*, *ELN*, *CCN1*, *FBLN5*	2024	Adelus et al.[75]
Carotid arteries	By genes: *MAFB*, *SULF1*, *RAB3C*, *MAF*, *PGF*, *SEMA3G*	2023	Tan et al.[50]
Carotid and coronary arteries	Classical ECs: *PECAM1*, *CLDN5*; Intimal ECs: *RAMP2*; Pro-angiogenic ECs: *ACKR1*, *AQP1*, *FABP4*; Pro-inflammatory ECs: *SELE*, *CCL2*; EndMT ECs: *COL1A2*, *FN1*	2023	Verdezoto et al.[5]
Coronary arteries	EC00: *CA4*, *GPIHBP1*, *LPL*, *CD36*, *RGCC*; EC01: *ACKR1*, *POSTN*, *ICAM1*, *CCL14*, *VCAM1*; EC02: *FTL*, *FTH1*, *TMSB4X*; EC04: *GJA4*, *PCSK5*, *COL8A1*, *DKK2*	2023	Fu et al.[85]
Coronary arteries	EndMT-angiogenesis: *FN1*, *COL8A1*, *COL3A1*, *BGN*, *MMP2*, *EDN1*; EndMT-SMC contraction: *ACTA2*, *TAGLN*, *LUM*, *DCN, CALD1*	2022	Gole et al.[86]
Carotid arteries	EC-AC: *DKK2*, *FN1*, *F5*, *ITLN1*; EC-PA: *ACKR1*, *IL6*, *MLPH*, *HLA-DQA1*	2022	Alsaigh et al.[8]
Coronary arteries	EC01 (Pro-inflammatory): *ACKR1*, *CCL14*, *PLVAP*, *SELE*, *IL6*; EC02 (Developing): *SEMA3G*, *HEY1*, *CLDN5*, *CXCL12*; EC03 (SULF1^{+}): *ITLN1*, *MGP*, *EDN1*, *SULF1*	2021	Hu et al.[9]
Carotid arteries	EC00: *ACKR1*; EC01: *BMP4*; EC02: *FGF18*; EC03: *ACTA2*	2020	Depuydt et al.[87]

EC endothelial cell, *EndMT* endothelial-to-mesenchymal transition, *SMC* smooth muscle cell, *AC* atherosclerotic core, *PA* proximal adjacent.

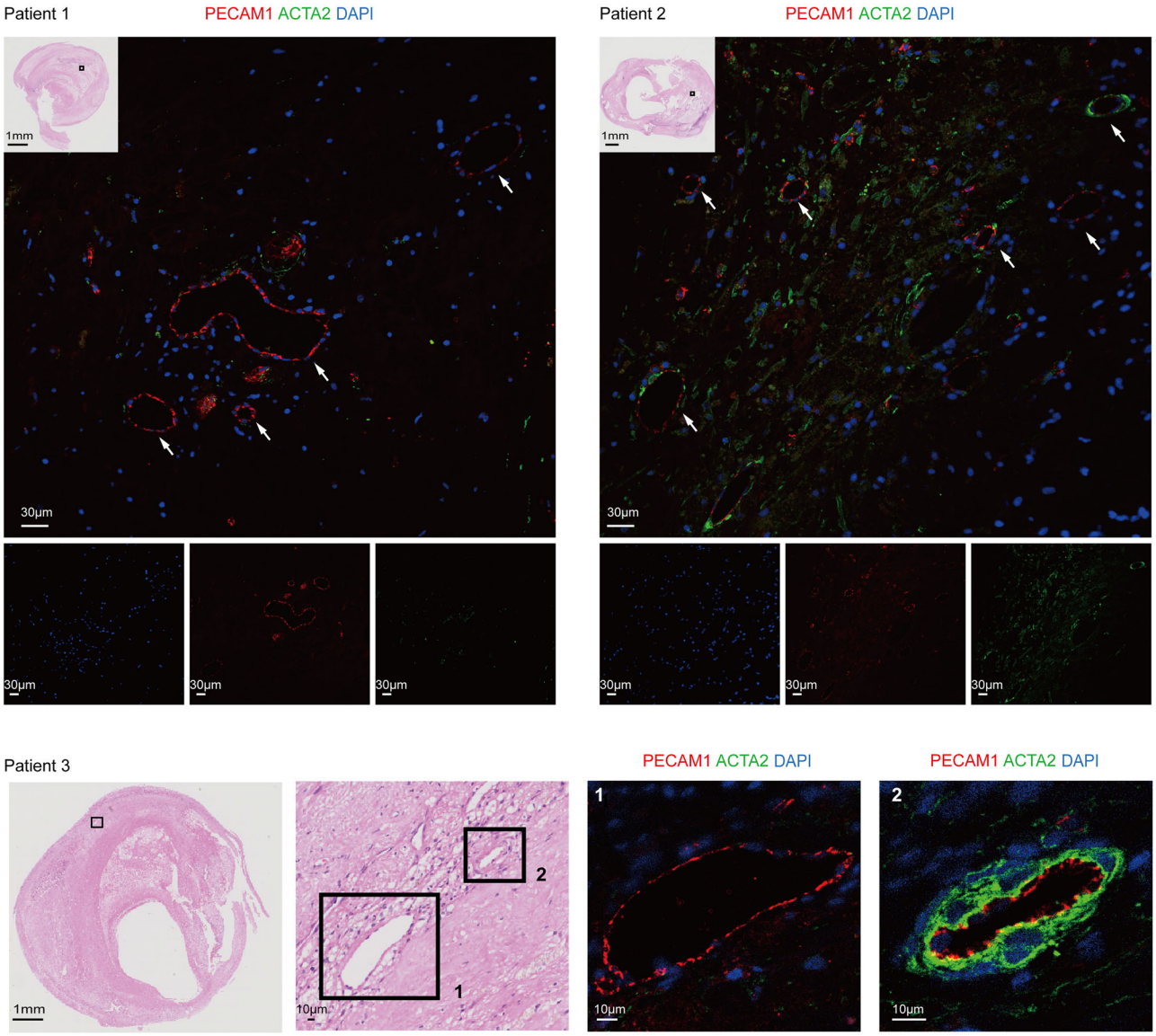

Fig. 1 | H&E and immunofluorescence (PECAM1/ACTA2) from the same carotid plaque region in each patient (Patients 1–3). Representative images of human carotid endarterectomy plaques from Qilu Hospital (Supplementary Table 2). For each patient, H&E and immunofluorescence images of PECAM1 (red), ACTA2 (green), and DAPI (blue) were shown from the same plaque region on adjacent serial sections. Scale bars: H&E overview image, 1 mm; merged and single-channel immunofluorescence images for patients 1 and 2, 30 μm; H&E regional image and enlarged immunofluorescence images for patient 3, 10 μm.

associated with E01-veins-SELE and E02-veins-AQP1, and Module3 was linked to E01-veins-SELE and hypoxia-associated E04 subcluster (Fig. 3A; Supplementary Fig. 5A–D; Supplementary Data 2). E04, which was primarily derived from patients in Hu's cohort[9], originated from individuals without atherosclerotic lesions but who were in the end stage of heart failure[9] (Fig. 2C, E). Module1 was associated with complement activation and included the hub genes *C1R* and *C1S* (Fig. 3B; Supplementary Fig. 5C; Supplementary Data 2). Module2 and Module3 displayed a negative correlation with Module1, underscoring the distinct regulatory networks (Fig. 3C; Supplementary Data 2). Gene ontology (GO) enrichment analysis revealed that Module1 was enriched in biological processes related to artery morphogenesis, endothelial cell migration and the BMP signaling pathway (Fig. 3D; Supplementary Fig. 5C; Supplementary Data 2). The hub genes in Module2 were predominantly MHC class II molecules (Fig. 3B, D), while Module3 exhibited a distinct pro-inflammatory signature. *ICAM1* and *SELE*[22], known for their roles in leukocyte adhesion, were identified as central nodes within the Module3 network, which is functionally linked to lipid metabolism and cell death regulation (Fig. 3B, D). Furthermore, the expression of MHC class II molecules was predominantly enriched in E01-veins-SELE and E02-veins-AQP1, aligning closely with the distribution of *ACKR1* (Fig. 3E; Supplementary Fig. 5D). E01-veins-SELE had the highest score for MHC class II molecules (Fig. 3F; Supplementary Data 3). Endothelial cells lacked the expression of co-stimulatory receptors, indicating that they function as semi-professional antigen-presenting cells participating in immune modulation within atherosclerotic environments (Fig. 3F, G). Taken together, hdWGCNA distinguished different gene expression modules, which clustered within distinct endothelial cell types, each exhibiting a unique gene regulatory network.

Indications of the functional diversity of venous endothelial cells

Vascular endothelial dysfunction is characterized by impaired endothelium-dependent vasodilation, increased oxidative stress, chronic inflammation, enhanced leukocyte adhesion, hyperpermeability, and endothelial cell senescence[2]. Adhesion molecules and chemokines mediate leukocyte adhesion and direct migration[23]. To better understand the leukocyte adhesion capacity, we investigated expression patterns of

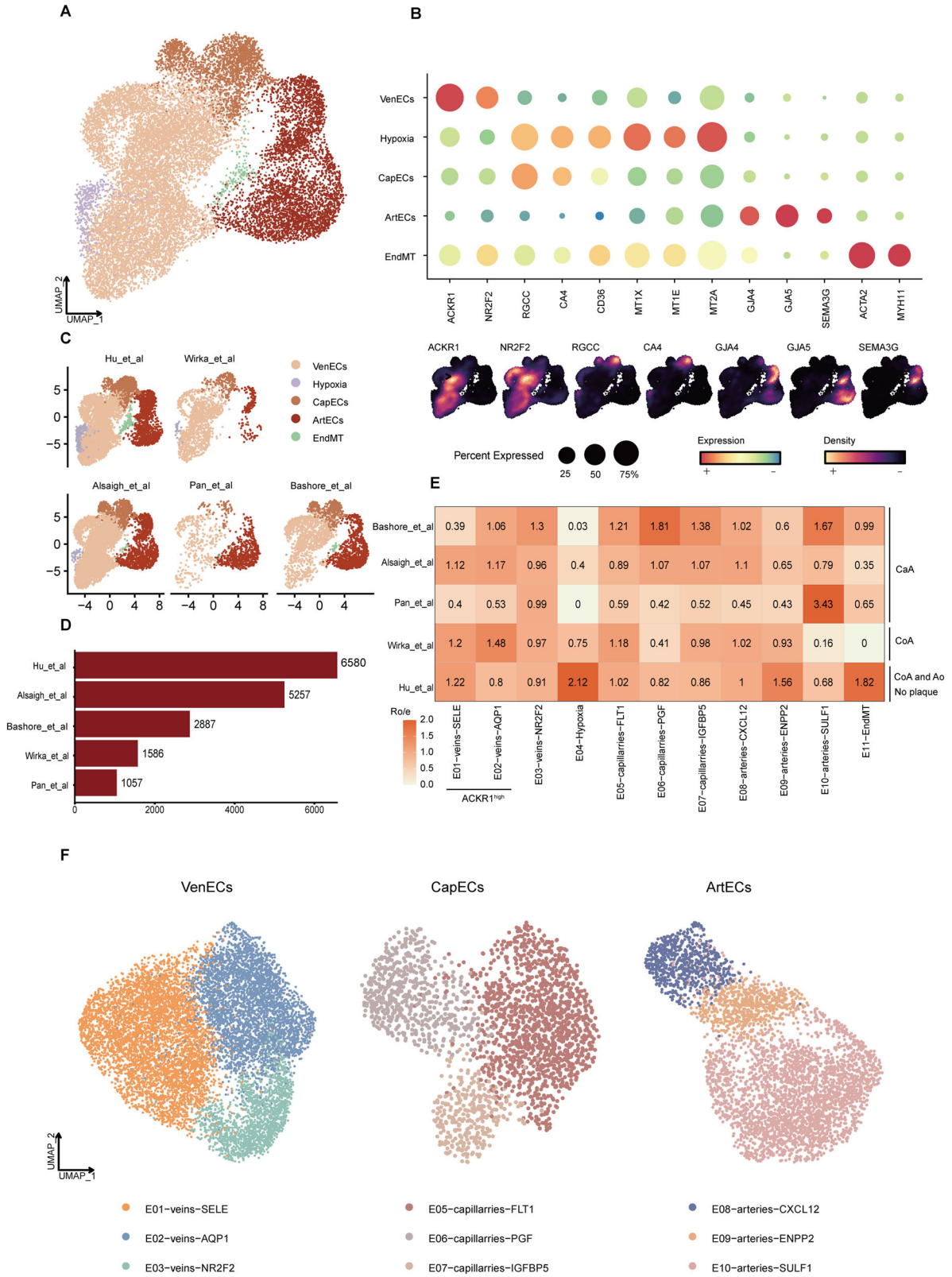

Fig. 2 | Landscape of atherosclerosis vascular endothelial cells at single-cell resolution. **A** Uniform manifold approximation and projection (UMAP) visualization displayed the major compartments of 17,367 VECs. **B** Dot plots and density scatter plots illustrating the expression patterns of corresponding signature genes for each cluster. The size of each dot indicates the proportion of cells expressing the gene, and the color represents gene expression levels. **C** UMAP plots of vascular endothelial cells across different cohorts. **D** Boxplots showing the number of vascular endothelial cells across different cohorts. **E** Heatmap showing the distribution of VECs subclusters across different cohorts based on the ratio of observed to expected (Ro/e) scores. CaA Carotid artery, CoA Coronary artery, Ao Aorta. **F** UMAP plots of all VECs subclusters within their major compartments.

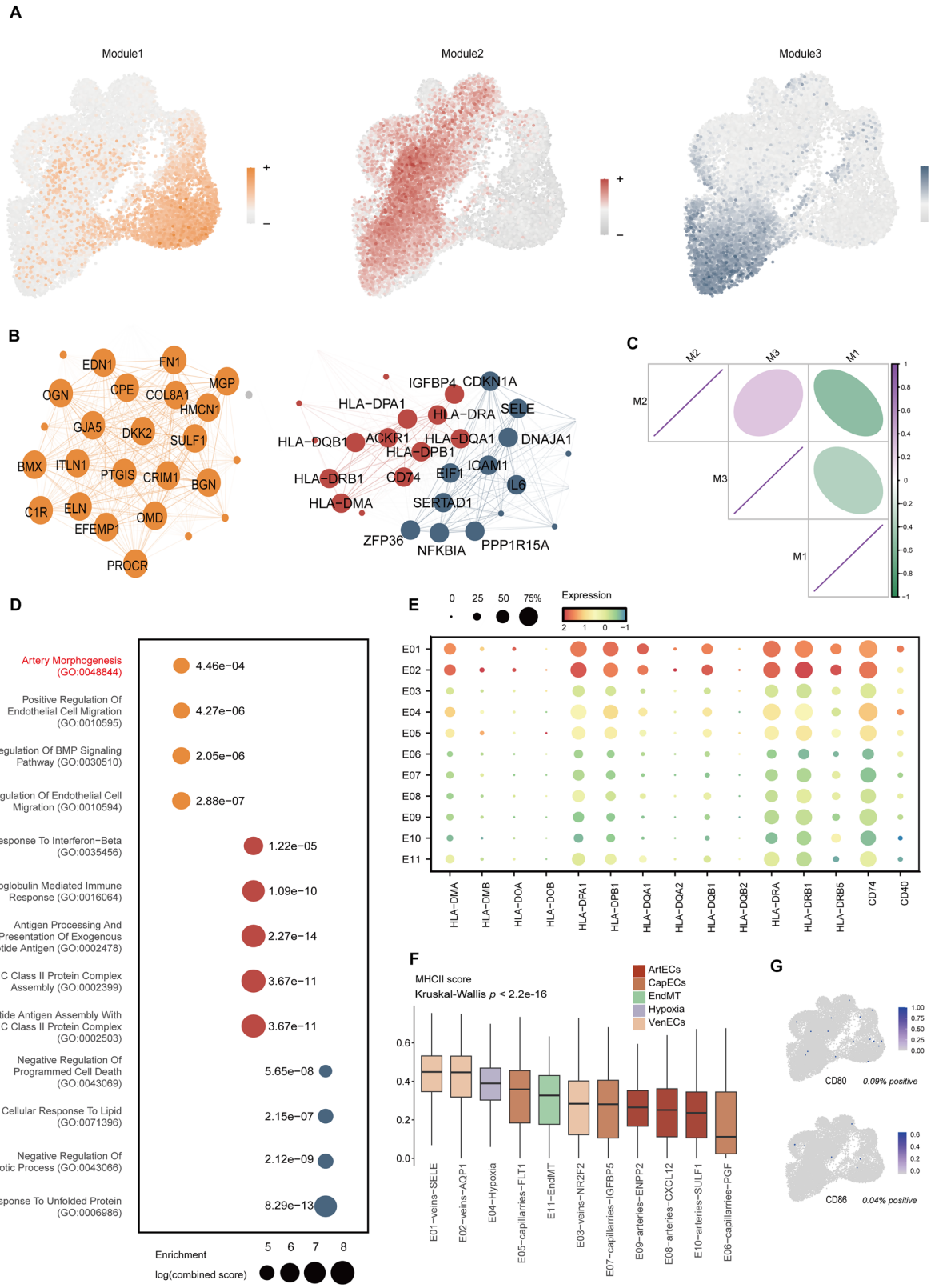

Fig. 3 | hdWGCNA reveals distinct differences among VECs subclusters. **A** UMAP plots of three gene co-expression modules identified through hdWGCNA. **B** Density scatter plots illustrating the expression patterns of corresponding signature genes for each module. **C** The correlation between modules based on Pearson correlation analysis (M1: Module1; M2: Module2; M3: Module3). Pearson correlation coefficients (r) are represented by a color gradient, ranging from green (negative correlation) to purple (positive correlation). **D** GO enrichment analysis of each hdWGCNA module. For each non-gray module, the hub genes were tested with RunEnrichr (hdWGCNA). **E** Dot plots illustrating the expression patterns of MHC class II signature genes for VEC subclusters. **F** Boxplots comparing the AUCell scores of MHC class II among all VECs subclusters. Kruskal–Wallis test. **G** Featureplots showing the expression of co-stimulatory molecules *CD80* and *CD86*.

chemokines and adhesion molecules across VECs subclusters. E01-veins-SELE exhibited the highest leukocyte adhesion capacity, followed by E10-arteries-SULF1 (Fig. 4A). Notably, the E10-arteries-SULF1 showed high expression of *SELP*, while E01-veins-SELE exhibited elevated levels of *SELE*, *ICAM1*, and *VCAM1*, along with key chemokines *CCL2*, *CXCL2*, and *CXCL8*, suggesting distinct roles in leukocyte recruitment and inflammatory responses[22] (Fig. 4A, B; Supplementary Data 3).

E01-veins-SELE represents a VenECs subcluster characterized by high expression of *ACKR1* and low expression of *NR2F2*. Immunofluorescence staining revealed the existence of two distinct VenECs subclusters based on ACKR1 and NR2F2 (Fig. 4C; Supplementary Fig. 4B). Interestingly, even among *ACKR1*^{high} cells, significant heterogeneity was observed, with E01-veins-SELE emerging as the primary inflammatory cluster, whereas E02-veins-AQP1 contributed to endothelial development and exhibited high expression of *TXNIP*, which is essential for maintaining endothelial cell function in metabolic disorders[24] (Fig. 4D, E; Supplementary Data 1). These differential expression patterns provided insight into the distinct yet interconnected gene regulatory networks of the Module2 and Module3 (Fig. 3A; Supplementary Fig. 5D). Moreover, *ACKR1*^{low}*NR2F2*^{high} E03-veins-NR2F2 highly expressed *PLAT* (tissue-type plasminogen activator, tPA) and *POSTN* (Fig. 4E). tPA plays a critical role in fibrin degradation[25], suggesting that E03-veins-NR2F2 was the subcluster involved in thrombus resolution within the plaque microenvironment. GO enrichment revealed that E03-veins-NR2F2 mainly were involved in wound healing (Fig. 4F; Supplementary Data 1). E01-veins-SELE exhibited NF-κB pathway activation, with transcription factors *EGR1* and *ETS2* being upregulated (Fig. 4G, H). The activation of *EGR1* induces endothelial inflammation[26], while *ETS2* contributes to atherosclerotic plaque destabilization by promoting an inflammatory endothelial cell phenotype[27]. VECTOR analysis further revealed VenECs state trajectory, indicating that they acquire distinct inflammatory and tissue repair characteristics over time (Fig. 4I).

These results highlighted the functional diversity of VenECs subclusters with specialized roles in inflammation and tissue repair. While *ACKR1*^{high} cells exhibited high expression of MHC class II molecules, they displayed two distinct subclusters in inflammatory responses. E02-veins-AQP1 was more associated with endothelial homeostasis, whereas E01-veins-SELE exhibited pro-inflammatory characteristics. Additionally, the *ACKR1*^{low}*NR2F2*^{high} E03-veins-NR2F2 played a role in wound healing and could contribute to thrombus resolution through high expression of *PLAT*.

Angiogenesis in atherosclerotic plaque

Sprouting angiogenesis has been identified as the primary mechanism of neovascularization in atherosclerosis[28]. To elucidate the key cellular clusters and molecular mechanisms underlying intraplaque neovascularization, we first assessed the sprouting capacity of endothelial cells by analyzing an angiogenesis score. E05-capillaries-FLT1 and E06-capillaries-PGF exhibited higher angiogenic activity (Fig. 5A; Supplementary Data 3). The principal regulatory receptors of vascular sprouting, VEGFR1 (encoded by *FLT1*) and VEGFR2 (encoded by *KDR*)[29], were predominantly expressed in E05-capillaries-FLT1, underscoring their role in initiating angiogenesis (Fig. 5B). In contrast, the E06-capillaries-PGF displayed elevated expression of a tip cell marker, Apelin[16] (encoded by *APLN*) (Supplementary Fig. 6A). To reconstruct the trajectory of atherosclerosis-associated angiogenesis, we designated the VEGFR1-high and VEGFR2-high expression region within E05-capillaries-FLT1 as the root state, revealing two distinct differentiation pathways of capillary endothelial cells (Fig. 5B; Supplementary Fig. 6B, C). Trajectory 1 revealed the transition from stalk-like to tip-like capillary endothelial cells (Fig. 5C, D). Based on Trajectory 1, we defined three critical time points: (i) the lowest tip-cell score (S_t) (x = 5.68), (ii) the highest stalk-cell score (S_s) (x = 7.35), and (iii) the transition point where S_t and S_s intersect (x = 12.36). After time point (ii), the cells were only in the process of transforming into tip cells and lost stalk cell characteristics. E05-capillaries-FLT1 exhibited high expression of *TGFBR2*, while *TGFBR1* remained at a low expression level, emphasizing the initiating role of the TGF-β signaling pathway in vascular sprouting[30] (Fig. 5E; Supplementary Fig. 6D). Conversely, the terminal cells of Trajectory 2 (E07) exhibited high expression of *IGFBP5*, an angiogenesis inhibitor[31], along with *TEK* (also known as Tie2), which is involved in angiogenic regulation and vascular stability maintenance[16,32] (Fig. 5E). These two distinct trajectories illustrated the fate of CapECs, highlighting the intricate regulatory mechanisms governing angiogenesis in atherosclerosis. We aimed to dissect the gene regulatory network underlying capillary-like endothelial neovascularization through Trajectory 1. Multiple vascular regulators, including *PGF*, *ADM*, *APLN*, *ANGPT2*, *THBS1*, and *PDGFB*, orchestrated angiogenic processes[33–38] (Fig. 5F). Endothelial-derived CXCL12 has been implicated in atherosclerosis progression, with its function varying depending on CXCR4 distribution[39]. In this study, we identified E08-arteries-CXCL12 as the primary endothelial cluster expressing *CXCL12* (Supplementary Fig. 6E). Tip-like endothelial cells predominantly expressed *CXCR4* and could facilitate angiogenesis by responding to *CXCL12*[40] (Supplementary Fig. 6E). Furthermore, extracellular matrix (ECM) components such as *COL4A1*, *COL4A2*, *LAMA4*, *LAMB1*, and *LAMC1*, which contribute to cell adhesion and microenvironment homeostasis, were upregulated during the transition toward tip-like endothelial cells, facilitating dynamic ECM remodeling[41] (Fig. 5F). *SMAD1* and *INHBB* regulate angiogenesis through the BMP/TGF-β signaling pathway and exhibit increased expression during tip-like cell formation[42] (Fig. 5F). Vimentin (encoded by *VIM*) could play a role in regulating cell adhesion and facilitating endothelial sprouting[43] (Fig. 5F). *FSCN1* regulates cytoskeletal reorganization, promoting filopodia formation and enhancing endothelial cell migration[44] (Fig. 5F). NOTCH signaling pathway was activated at the starting point and was reactivated during tip cell formation, regulating angiogenesis and potentially preventing excessive vascular growth[45] (Fig. 5G). *ENG*, *PIK3R3*, and *PLPP1* exhibited sustained downregulation throughout this process, whereas *RAMP2*, *RAMP3*, and *CALCRL* were upregulated early on, suggesting that adrenomedullin (ADM) may play a crucial role in the initial stages of endothelial cell transition[34]. Pathway enrichment analysis further revealed that E06-capillaries-PGF exhibited activation of the MAPK, VEGF, WNT, and hypoxia signaling pathways, while TGF-β signaling was predominantly enriched in E05-capillaries-FLT1 (Fig. 5H).

Transcription factor analysis corroborated the involvement of known angiogenesis regulators. *HIF1A* and HIF2A (encoded by *EPAS1*) exhibited different expression patterns, while *KLF2*, a key factor in vascular stability, demonstrated reduced expression during angiogenesis[46] (Fig. 5I; Supplementary Fig. 6F, G). *ID1*[47] was upregulated in the early stages, whereas *TCF4*[48] was gradually activated in E06-capillaries-PGF (Fig. 5I; Supplementary Fig. 6F, G). Although all these transcription factors contributed to angiogenesis, they exhibited distinct expression patterns, reflecting their specialized roles in endothelial cell dynamics. However, research on *TSC22D1* remained limited.

These results revealed the major endothelial cell subclusters, with E05-capillaries-FLT1 and E06-capillaries-PGF representing key populations involved in sprouting angiogenesis, and highlighted how these subclusters may interact through the CXCL12/CXCR4 axis.

Endothelial-to-mesenchymal transition

Endothelial-to-mesenchymal transition (EndMT) has been implicated in the progression of atherosclerosis by contributing to endothelial dysfunction[49]. Our previous study has also elucidated that PIM1 promotes the progression of atherosclerosis by inducing endothelial-to-mesenchymal transition[14]. To systematically characterize endothelial clusters undergoing mesenchymal transition, endothelial cell marker genes and EndMT-associated genes were integrated to compute $R_{M/E}$ scores (Methods). Among the identified subclusters, E10-arteries-SULF1 and E11-EndMT exhibited $R_{M/E}$ scores exceeding 1, indicating mesenchymal-like cells (Fig. 6A; Supplementary Data 3). E11-EndMT, marked by high expression of *ACTA2*, *TAGLN*, and *MYH11*, exhibited a distinct transcriptional profile from E10-arteries-SULF1, which expressed high levels of *FN1*, *BGN*, *ELN*, and *COL8A1*, highlighting the heterogeneity within mesenchymal-like endothelial cell subclusters (Supplementary Fig. 7A). E10-arteries-SULF1

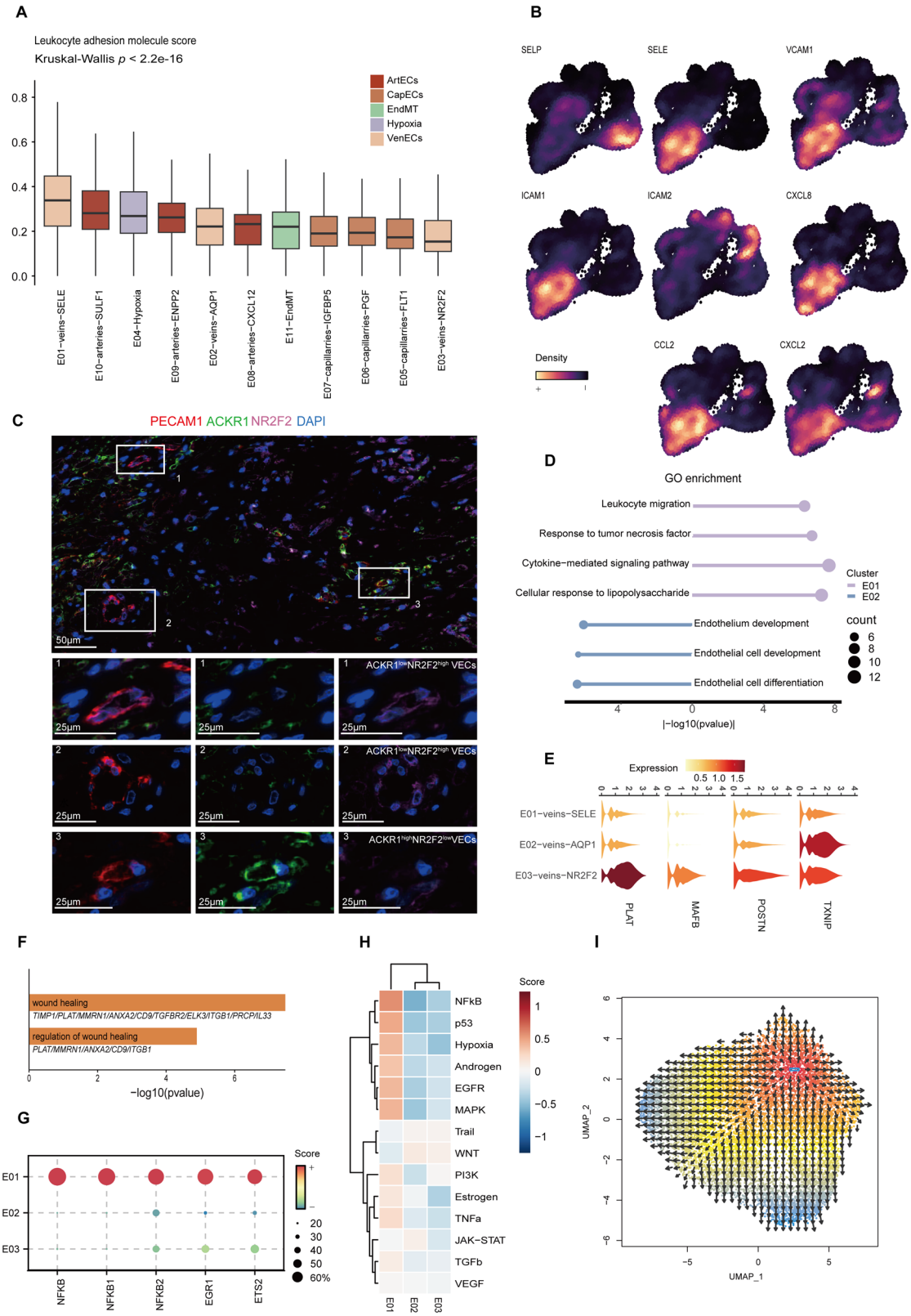

Fig. 4 | The functional heterogeneity of venous endothelial cells. A Boxplots comparing the AUCell scores of leukocyte adhesion molecules among VECs subclusters. Kruskal–Wallis test. **B** Density scatter plots of adhesion molecules and chemokines. **C** Representative immunofluorescence images of human carotid endarterectomy plaques from Qilu Hospital (patient 4; Supplementary Table 2) showing the expression and localization of ACKR1 and NR2F2. Nuclei were counterstained with DAPI. Scale bars: 50 μm in the overview image; 25 μm (1, 2 and 3). **D** GO enrichment analysis of E01 and E02 subclusters. **E** Violin plots showing gene expression patterns. The color represents gene expression levels. **F** GO enrichment analysis of E03 subcluster. **G** Dot plots illustrating transcription factor activity. The size of each dot indicates the proportion of cells with transcription factor activity > 0, and the color represents the activity level score. **H** Heatmap showing pathway activity using decoupleR. **I** The vector representation of developmental directions for cells in VenECs, by using VECTOR. The pseudotime order of cells is shown by color (from red to blue).

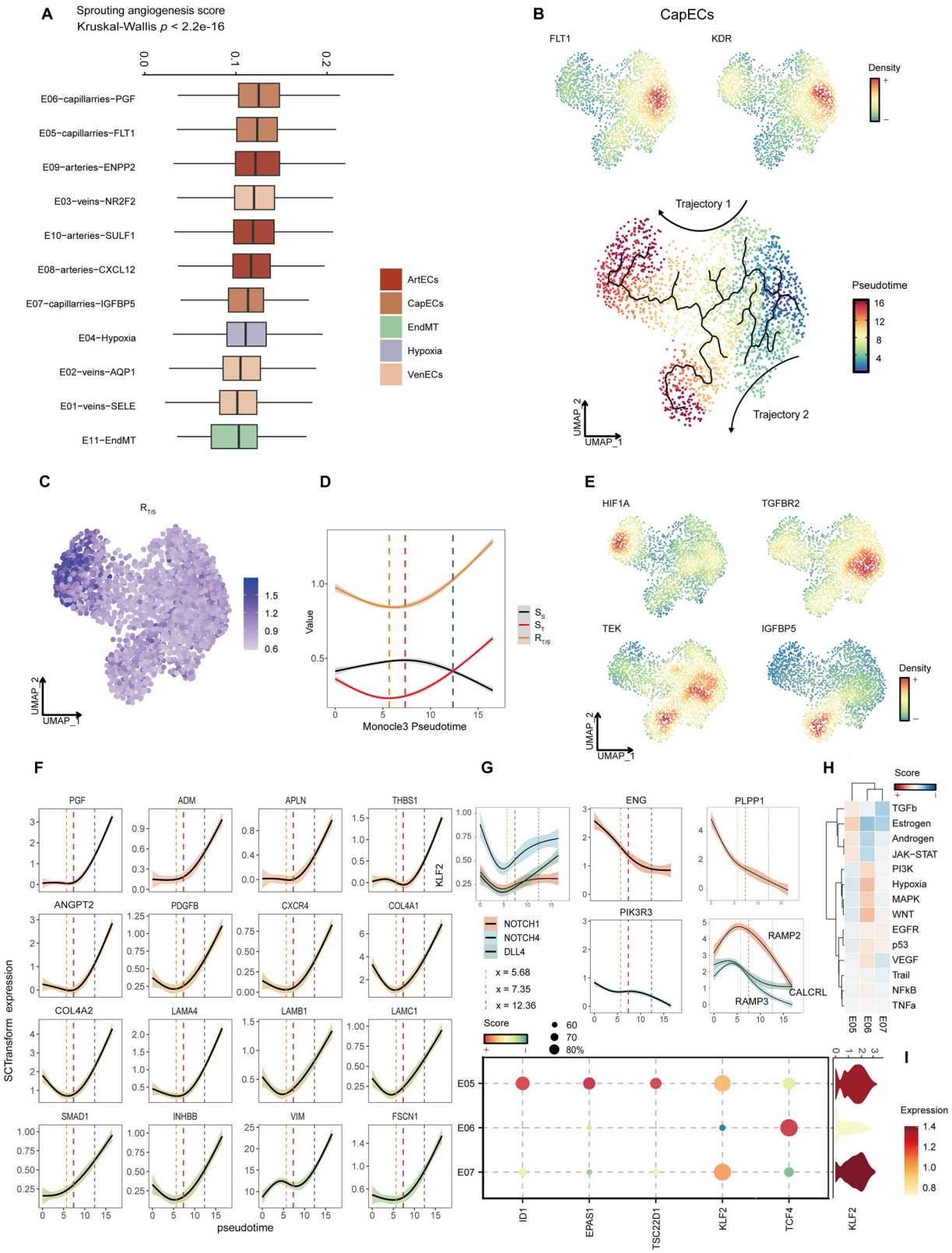

Fig. 5 | Angiogenesis in atherosclerotic plaques. A Boxplots comparing the AUCell scores of sprouting angiogenesis among all VECs subclusters. Kruskal–Wallis test. **B** Density scatter plots of *FLT1* and *KDR*, and a UMAP plot showing the pseudotime trajectory calculated with Monocle3 in CapECs. The arrows indicate two distinct developmental trajectories. **C** UMAP plots showing $R_{T/S}$. **D** Cubic spline interpolation of S_S, S_T and $R_{T/S}$ across pseudotime with 95% confidence intervals. **E** Density scatter plots of *HIF1A*, *TGFBR2*, *TEK* and *IGFBP5*. **F**, **G** Cubic spline interpolation of gene expression across pseudotime with 95% confidence intervals. **H** Heatmap showing pathway activity using decoupleR. **I** Dot plots illustrating transcription factor activity. The size of each dot indicates the proportion of cells with transcription factor activity > 0, and the color represents the activity level score. Violin plots showing *KLF2* expression patterns. The color represents gene expression levels.

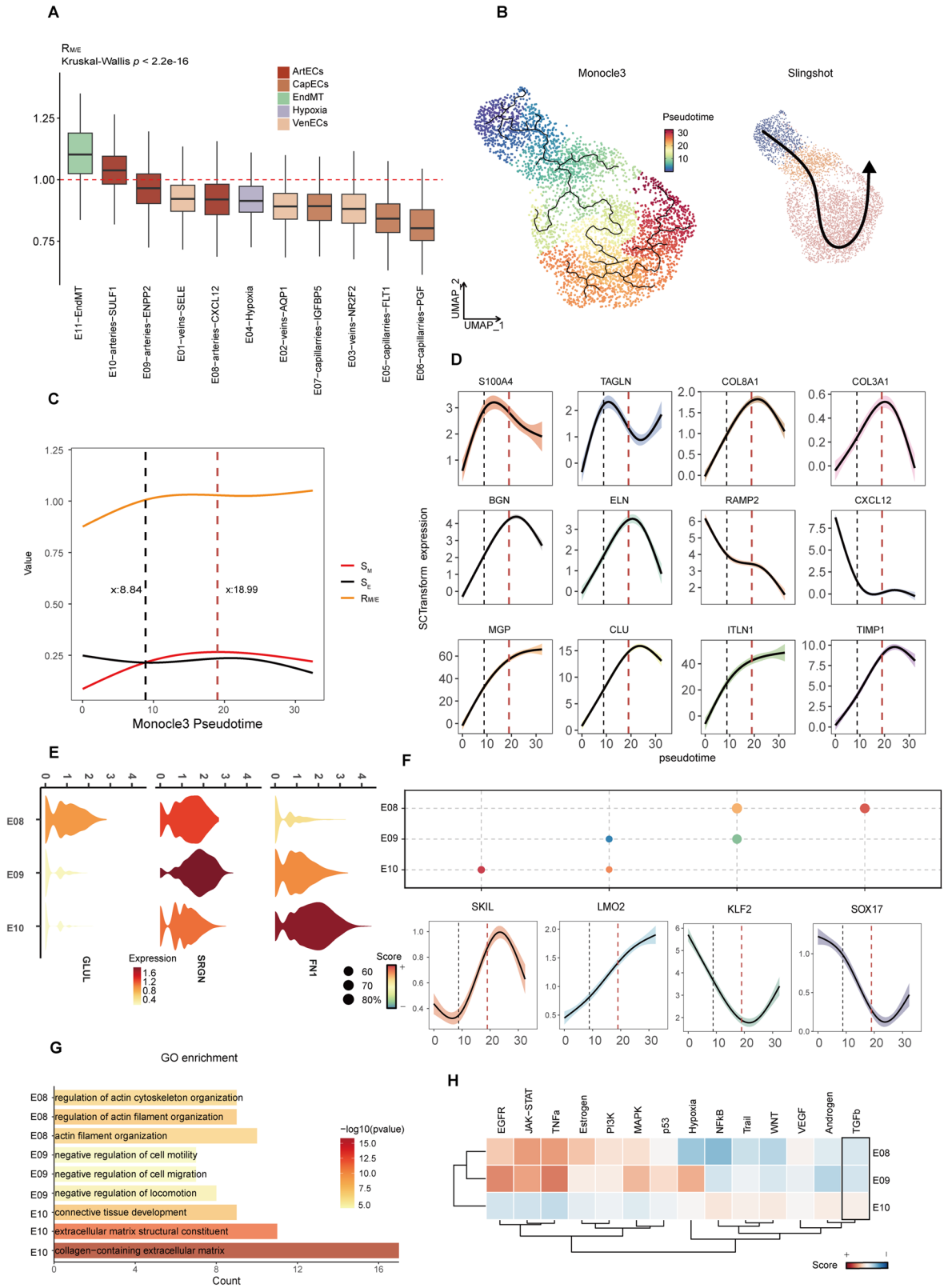

Fig. 6 | Endothelial-to-mesenchymal transition in atherosclerotic plaques. **A** Boxplots comparing $R_{M/E}$ among all VECs subclusters. Kruskal–Wallis test. **B** UMAP plots showing the pseudotime trajectory calculated with Monocle3 and Slingshot in ArtECs. **C** Cubic spline interpolation of S_M, S_E and $R_{M/E}$ across pseudotime with 95% confidence intervals. **D** Cubic spline interpolation of gene expression across pseudotime with 95% confidence intervals. **E** Violin plots showing gene expression patterns. The color represents gene expression levels. **F** Dot plots illustrating transcription factor activity. The size of each dot indicates the proportion of cells with transcription factor activity >0, and the color represents the activity level score. Cubic spline interpolation of TFs expression across pseudotime with 95% confidence intervals. TFs transcription factors. **G** GO enrichment analysis of E08, E09 and E10 subclusters. **H** Heatmap showing pathway activity using decoupleR.

was broadly distributed across multiple datasets (Fig. 2D), with *SULF1*$^+$ VECs displaying the lowest correlation with other endothelial clusters[50] (Supplementary Fig. 7B, C). It was identified as a key endothelial cluster undergoing EndMT. ArtECs and the inflammatory endothelial subcluster E01-veins-SELE were among the top-ranked clusters based on $R_{M/E}$ (Fig. 6A). To further investigate the cell state trajectory of E10-arteries-SULF1, pseudotime trajectory analysis was performed. E08-arteries-CXCL12, the subcluster with the lowest $R_{M/E}$ in ArtECs, was selected as the starting point. Monocle3 and Slingshot generated consistent trajectories, identifying distinct cell state transitions (Fig. 6B). VECTOR analysis distinguished two cellular states, corresponding to the terminal states and branching points identified by Monocle3 (Supplementary Fig. 7D). Following the transition to mesenchymal-like cells ($R_{M/E} = 1$, x = 8.84, Point1), the mesenchymal-like cell score peak was identified as the next key inflection point (x = 18.89, Point2), beyond which the expression of multiple mesenchymal markers declined (Fig. 6C, D). Using Monocle3, gene expression dynamics along the pseudotime trajectory were modeled, revealing a progressive increase in mesenchymal marker expression (*S100A4*, *TAGLN*, *ELN*, and *BGN*) during EndMT (pseudotime range: 0–8.84), while *RAMP2*[5], a homeostatic EC marker, and E08-arteries-CXCL12 specific marker *CXCL12* decreased, indicating a shift in cell state (Fig. 6D; Supplementary Fig. 7E). The loss of *RAMP2* promotes the transition to mesenchymal cells[51]. *VIM* displayed an intriguing expression pattern (Supplementary Fig. 7F). Concurrently, several endothelial markers (*PECAM1*, *CDH5*, *VWF, and TEK*) demonstrated significant downregulation after Point2, suggesting alterations in endothelial phenotypic characteristics (Supplementary Fig. 7E). Interestingly, *PECAM1* expression increased prior to Point 1 (Supplementary Fig. 7E). Such upregulation of *PECAM1* has also been observed in in vitro experiments of EndMT[52].

Further analysis revealed a marked increase in the expression of *MGP*, *CLU*, *ITLN1*, and *TIMP1* (Fig. 6D). The role of high *CLU* expression in endothelial cells remains to be fully elucidated, but reduced secretory clusterin (encoded by *CLU*) could inhibit the migration of HUVECs[53]. MGP inhibits vascular calcification[54], while ITLN1, an inhibitor of the TGF-β pathway[55], suggested a negative feedback mechanism. TIMP1, a matrix metalloproteinase (MMP) inhibitor, prevents tissue collagen degradation[56]. Differential gene expression analysis identified *SRGN* and *GLUL* as dynamically regulated genes (Fig. 6E). *SRGN*, a shear-stress-responsive gene[57], was highly expressed in the E09-arteries-ENPP2 (Fig. 6E). Glutamine synthetase (encoded by *GLUL*), involved in glutamine metabolism, lost expression during the transition to mesenchymal-like cells (Fig. 6E).

Pathway and transcription factor analyses further delineated distinct functional characteristics of ArtECs. *SKIL*, a negative regulator of TGF-β signaling[58], was enriched in E10-arteries-SULF1, whereas *KLF2*, a key factor maintaining ECs stability[59], was downregulated. Evidence that *SOX17* was functionally active in E08-arteries-CXCL12 was found, but its expression declined as cells transitioned to a mesenchymal-like state (Fig. 6F). GO enrichment analysis revealed that E08-arteries-CXCL12 exhibited high expression of cytoskeletal regulation genes, whereas E09-arteries-ENPP2 showed enrichment for genes negatively regulating cell migration, including *CLDN5*, *IGFBP3*, *IFITM1*, *DUSP1*, *MCTP1*, *IL33* and *RHOB* (Fig. 6G; Supplementary Data 1). In contrast, *LMO2*, a regulatory factor of endothelial cell migration[60], was significantly upregulated in E10-arteries-SULF1, suggesting a higher migratory potential (Figs. 3D and 6F; Supplementary Fig. 7G). Pathway scoring further indicated higher TGF-β signaling activity in E10-arteries-SULF1, consistent with its role in EndMT progression (Fig. 6H). Following SULF1 overexpression, the surface expression of the endothelial marker CD144[61] on HUVECs was reduced (Supplementary Fig. 8A–C; Supplementary Data 4). Immunofluorescence revealed endothelial cells characterized by SULF1 and PECAM1 expression in vasa vasorum in the plaque (Supplementary Fig. 8D).

These findings collectively defined *SULF1*$^+$ endothelial cells as a major endothelial cluster undergoing EndMT within atherosclerotic plaques. Multiple factors regulate this transition, and distinct gene expression dynamics characterize the endothelial-to-mesenchymal transition process, accompanied by the downregulation of endothelial-specific markers.

Discussion

In this study, we present a comprehensive single-cell transcriptomic atlas of endothelial cells (ECs) within human atherosclerotic plaques, integrating data from multiple vascular beds across diverse cohorts. We prioritized datasets that (1) report unambiguous tissue origins directly relevant to atherosclerosis, (2) feature well-defined cell types and high data quality (Supplementary Fig. 1), enabling accurate identification of vasa vasorum–related endothelial subclusters, and (3) are publicly available and have been widely used in previous studies[5,62,63]. This cross-study integration allows for a deeper analysis, uncovering biological patterns that might be overlooked in single-cohort studies[64]. By systematically resolving endothelial heterogeneity at single-cell resolution, we uncovered novel subclusters with distinct transcriptional and functional characteristics, highlighting the complex landscape of endothelial adaptation in the atherosclerotic microenvironment.

Our work refined classification of vascular endothelial cells (VECs) into arterial (ArtECs), venous (VenECs), and capillary-like (CapECs) subtypes, further stratified into 11 unique subclusters. Among these, *ACKR1*^{high} endothelial cells were identified as venous-type ECs characterized by robust expression of MHC class II molecules while lacking co-stimulatory signals, suggesting a role as semi-professional antigen-presenting cells involved in modulating local immune responses. Notably, substantial heterogeneity was observed within the *ACKR1*^{high} cluster. The E01-veins-SELE subcluster exhibited a strong pro-inflammatory profile, marked by high expression of adhesion molecules such as *SELE*, *ICAM1*, and *VCAM1*, indicative of an activated endothelium that promotes leukocyte recruitment. E03-veins-NR2F2, exhibiting relatively low expression of *ACKR1*, demonstrated a reparative phenotype characterized by upregulation of *NR2F2* and *PLAT*. Through high-dimensional weighted gene co-expression network analysis (hdWGCNA), we delineated three distinct regulatory modules. Particularly, Module3, enriched in SELE, *ICAM1*, and *CXCL8*, underpinned the immune-activated signature of E01-veins-SELE, while Module1 was dominant in ArtECs and associated with vessel morphogenesis and BMP signaling.

Another finding is the dissection of angiogenic dynamics within capillary-like endothelial cells. Trajectory analysis revealed two distinct sprouting paths, driven respectively by VEGF signaling, and culminating in either tip-cell differentiation or stabilization by angiogenesis inhibitors, such as *IGFBP5*. The distinct activation of MAPK, WNT, and hypoxia pathways in clusters E06 versus TGF-β signaling in E05 underscores the multifaceted nature of neovascularization in plaques. Furthermore, the role of CXCL12/CXCR4 signaling in guiding angiogenic endothelial migration adds an additional layer of complexity to vascular remodeling.

We also identified *SULF1*$^+$ VECs as a major subcluster undergoing endothelial-to-mesenchymal transition (EndMT), a process strongly linked to plaque progression and instability. SULF1 promotes EndMT by enhancing TGF-β2 expression and signaling while simultaneously inhibiting FGF-mediated anti-EndMT effects[65–67]. *SULF1*$^+$ VECs have been found to be associated with plaque vulnerability in patients with cerebrovascular events[50]. Pseudotime analysis showed a sequential loss of endothelial identity (e.g., *VWF*, *PECAM1*) and acquisition of mesenchymal markers (e.g., *ACTA2*, *TAGLN*), alongside TGF-β pathway activation. Importantly, the identification of intermediate phenotypic states and the upregulation of negative feedback regulators (e.g., *ITLN1*) suggested that EndMT is a gradual, reversible process, potentially offering new therapeutic intervention windows.

Compared to previous studies focusing on bulk tissue or limited endothelial subtypes, our study provides a systematic, multi-cohort, high-resolution characterization of endothelial states in atherosclerosis. This comprehensive landscape not only validates known features (e.g., EndMT, inflammatory activation) but also reveals previously unrecognized

regulatory modules and cellular subsets with distinct functional potential. The use of integrative trajectory inference, co-expression network analysis, and pseudotime modeling further strengthens the mechanistic insights into endothelial dynamics.

There are several limitations to this study. The cross-sectional nature of atherosclerotic plaque analysis restricts temporal resolution of endothelial transitions. While integration across cohorts enhances generalizability, inter-sample variability and technical artifacts may influence cluster resolution. Future studies incorporating spatial transcriptomics and lineage tracing in animal models will be critical to validate the developmental origin and functional relevance of the identified clusters.

In conclusion, our findings underscore the phenotypic and functional complexity of endothelial cells in atherosclerotic lesions. The identification of distinct inflammatory, reparative, angiogenic, and mesenchymal-like subclusters provides a new conceptual framework for understanding endothelial plasticity and its contribution to plaque progression. These insights may pave the way for the development of targeted therapies aimed at modulating specific endothelial states to restore vascular homeostasis in atherosclerosis.

Methods

Carotid atherosclerotic plaque patients

This study received approval from the Ethics Committee of Qilu Hospital (approval number KYLL-202111-037-1), and all participants provided written informed consent before enrollment. Patients aged 18 years or older who underwent carotid endarterectomy (CEA) for carotid artery stenosis or occlusion due to atherosclerosis between December 2020 and January 2023 were included. Diagnoses were confirmed, and other causes were excluded through Doppler ultrasound, computed tomography angiography (CTA), magnetic resonance imaging (MRI) or magnetic resonance angiography (MRA), and digital subtraction angiography (DSA). Clinical and demographic data were collected prior to CEA procedures. All ethical regulations relevant to human research participants were followed. Detailed clinical information for enrolled patients was provided in Supplementary Table 2.

Hematoxylin and eosin (H&E) staining

Carotid atherosclerotic plaque specimens were obtained from adult patients undergoing carotid endarterectomy at Qilu Hospital (December 2020–January 2023; Ethics Committee approval KYLL-202111-037-1, with written informed consent). After excision, tissues were fixed in 4% paraformaldehyde for 24 h, paraffin-embedded, and sectioned at 5 μm. Sections of carotid artery plaques were subjected to hematoxylin staining for 5 min, followed by rinsing with tap water until the nuclei appeared blue. Subsequently, eosin staining was performed for 3 min. The stained slides were then dehydrated through a graded ethanol series, cleared with an environmentally friendly clearing agent, and mounted using neutral balsam (G8590, Solarbio). High-resolution images were acquired using the WISLEAP Scanning System (WISLEAP Medical Technology Co., Ltd.), and plaque areas were quantitatively analyzed using NDP.view software (version 2.8.24).

Quality control and normalization of scRNA-seq sequencing libraries

Publicly available single-cell transcriptomic datasets of human atherosclerotic plaques include GSE159677 for the dataset from Alsaigh et al., GSE131780 for the dataset from Wirka et al., Zenodo (https://zenodo.org/record/6032099) for the dataset from Hu et al., GSE253903 for the dataset from Bashore et al., and GSE155512 for the dataset from Pan et al. The raw count matrices from each sequencing library across the five studies were obtained from GEO and Zenodo (Supplementary Table 1), and standardized processing was applied to all 38 sequencing libraries from 25 patients. Data preprocessing was conducted within the R programming environment (v4.2.3) using Seurat[68] (v4.4.0; https://github.com/satijalab/seurat). An initial round of clustering was performed using SCTransform normalization without filtering low-quality cells. To remove doublets, we employed the scDblFinder R package (v1.12.0)[69], which has demonstrated superior accuracy compared to other available tools, as indicated by recent benchmarking studies. Seurat objects were converted to SingleCellExperiment format and used as input for artificial doublet generation via scDblFinder's cluster-based modality. This approach constructs a k-nearest-neighbors graph incorporating both real cells and artificial doublets, estimating the density of doublets within each cell's neighborhood. Given the inherent variability in artificial doublet generation across different runs, we retained only consensus doublets identified in three independent iterations before eliminating the corresponding cell barcodes from the raw count matrices.

To mitigate the impact of ambient RNA contamination, a known issue in 10× Genomics protocols that can distort clustering and gene marker identification, DecontX from the celda R package (v1.6.1)[70] was applied to doublet-filtered raw count matrices under default parameters. The decontaminated count matrices generated by DecontX were then incorporated into Seurat objects. Quality control thresholds were subsequently applied to retain high-quality cells, defined as those with (1) between 200 and 4000 uniquely expressed genes, (2) between 200 and 20,000 unique molecular identifiers (UMIs), (3) ≤10% of total reads mapped to the mitochondrial genome, an indicator of compromised cell membrane integrity, and (4) ≤5% of total reads mapping to hemoglobin genes.

Following quality control, the raw count matrices were normalized using SCTransform. This normalization strategy has been demonstrated to enhance variable gene selection, dimensionality reduction, and differential expression analysis. To minimize clustering artifacts related to cell cycle effects, variance associated with cell cycle states was regressed out during SCTransform normalization. Dimensionality reduction was then performed using principal component analysis (PCA), and the first 30 principal components (PCs) were used for clustering via the shared-nearest-neighbor (SNN) graph and Louvain community detection algorithm in Seurat. Uniform Manifold Approximation and Projection (UMAP) was subsequently applied to visualize clustering results in a lower-dimensional space. The processed data matrices were ultimately stored as Seurat objects for subsequent batch correction. Gene expression density distributions were estimated using the Nebulosa[71] package.

Data integration and batch correction

We implemented three integration methods: rPCA (v4.4.0), Harmony (v1.0)[6], and scVI (v1.2.0)[72,73] to harmonize single-cell transcriptomic data. For Harmony integration, highly variable genes were identified and utilized for PCA-based dimensionality reduction, followed by batch correction using RunHarmony, with the corrected embeddings applied for clustering and visualization. In rPCA integration, PCA was independently performed on each library using 3000 highly variable genes, followed by dataset alignment via FindIntegrationAnchors, and subsequent clustering and UMAP visualization. For scVI integration, 3000 highly variable genes were selected per library, and batch correction was performed using a two-layer scVI model with a 30-dimensional latent space, generating a harmonized embedding for downstream analysis. To assess integration performance, we employed integration local inverse Simpson's index (iLISI) and cluster average silhouette widths (cASW).

iLISI score

We quantified the integration by calculating the integration local inverse Simpson's index (iLISI) using the compute_lisi function in the R package LISI, which reflected the effective number of datasets in a cell's neighborhood. Higher iLISI values indicated that neighborhoods were supplied by more datasets, resulting in a lower batch effect.

Cluster average silhouette widths

Silhouette coefficients are commonly used to evaluate the effectiveness and coherence of clustering results[5]. Under the assumption that each cluster represents a distinct cell type or subtype, we employed cASW to assess the biological conservation of clusters across different data integration methods, including rPCA, Harmony, and scVI. To compute cASW values, we extracted principal component analysis (PCA) embeddings from Seurat

objects processed with rPCA and Harmony, retaining the first 30 principal components (PCs). For scVI, instead of PCA-based embeddings, we utilized the latent space representations with n_latent = 30 (reduction = "scvi") as the default dimension, which provides a nonlinear representation of the data while mitigating batch effects. Using these embeddings, we constructed a Euclidean distance matrix via the stats R package. Cluster identities for individual cells were determined using FindNeighbors and FindClusters functions in Seurat, exploring a clustering resolution range from 0.1 to 1.5 in increments of 0.2. Across all tested resolutions, rPCA consistently achieved the highest cASW values (Supplementary Fig. 3D), suggesting that it better preserved the biological integrity of clusters compared to other integration methods.

For the annotation of endothelial cells, we selected 15 principal components (PCs) for computing silhouette widths to determine the optimal clustering resolution. These refined clusters were subsequently utilized for downstream analyses (Supplementary Fig. 3E).

Cell trajectory inference

To enhance the reliability of cell trajectory analysis, Monocle3, Slingshot, and Vector were employed, enabling cross-validation of inferred trajectories across multiple computational approaches. We finally used Monocle3 as the main method to infer gene expression changes over time.

Transcription factor and pathway activity using decoupleR

Transcription factor and pathway information were obtained separately using get_collectri and get_progeny (organism = 'human', top = 500), respectively[74]. Subsequently, transcription factor and pathway activities were assessed using run_ulm. When evaluating the activity of transcription factors in different subgroups, it is important to consider the expression levels of transcription factors. By intersecting with differentially expressed genes, the key differential transcription factors can ultimately be identified.

hdWGCNA analysis

Gene co-expression network analysis of vascular endothelial cell populations was performed using the hdWGCNA package (v0.4.0)[21]. To mitigate the sparsity inherent in single-cell transcriptomic data, hdWGCNA aggregates transcriptionally similar cells into metacells prior to network construction. A signed gene–gene adjacency matrix is then computed, which is subsequently transformed into a topological overlap matrix (TOM) to quantify network connectivity. Gene modules are identified through hierarchical clustering using the Dynamic Tree Cut algorithm and are summarized by module eigengenes (MEs), derived via singular value decomposition (SVD). After preparing the Seurat object for WGCNA, metacells were generated using the following parameters: k = 10, assay = 'SCT', max_shared = 5, min_cells = 300, reduction = 'umap', and slot = 'data'. Metacells were constructed by pooling only cells of the same type within the same sample. The ConstructNetwork function was then applied to build the co-expression network, using a soft-power threshold of 12. GO enrichment analysis for each module was performed using RunEnrichr.

Characterization of CapECs phenotypes

CapECs phenotypes were characterized by calculating tip-like (S_T) and stalk-like (S_S) scores using AUCell based on curated tip and stalk gene signatures[16]. $R_{T/S}$ was defined as $(S_T + 1) / (S_S + 1)$ and used to classify CapECs as tip-like cells or stalk-like cells[16].

Description of endothelial-to-mesenchymal transition

We first compiled gene signatures to define vascular endothelial cells (VECs) and mesenchymal cells derived from VECs[49,75–80]. The curated endothelial cell markers included *PECAM1*, *CDH5*, *VWF*, *COL4A1*, *COL4A2*, *KDR*, *FLT1*, *ESM1*, *TEK*, *KRT18*, *TJP1* and *TJP2*, while the mesenchymal cell markers consisted of *S100A4*, *FAP*, *TAGLN*, *ACTA2*, *VIM*, *MYH11*, *SMTN*, *CDH2*, *FN1*, *PDGFRA*, *COL1A1*, *COL1A2*, *SNAI1*, *SNAI2*, *BGN*, *ELN*, *CCN1*, *FBLN5*, *COL8A1*, and *COL3A1*.

To quantitatively assess the extent of endothelial and EndMT phenotypes, we applied a gene set enrichment-based supervised classification method using the AUCell[18] package in R, calculating both the endothelial score (S_E) and mesenchymal score (S_M). We then determined the ratio as $R_{M/E} = (S_M + 1) / (S_E + 1)$, where VECs with $R_{M/E} > 1$ were classified as mesenchymal-like cells.

Cell culture and overexpression

Human Umbilical Vein Endothelial Cells (HUVECs) were provided as a gift from the Department of Cardiology, Qilu Hospital of Shandong University, and cultured at 37 °C in 5% CO_2 in Endothelial Cell Medium (Catalog No. 1001, Science Cell) supplemented with 15% fetal bovine serum (FBS) (Catalog No. 0025, Science Cell), 1% Endothelial Cell Growth Supplement (ECGS, Catalog No. 1052, Science Cell), and 1% penicillin/streptomycin solution (P/S, Catalog No. 0503, Science Cell). For transient overexpression, HUVECs were seeded in antibiotic-free complete endothelial medium at 60-70% confluence one day before transfection. Cells were transfected with a human SULF1 expression plasmid (Homo-SULF1-NM_015170.3-FLAG-C in PCMV; empty vector as control) using Lipofectamine 3000 and P3000 reagent (Thermo Fisher Scientific, Cat. L3000008) according to the manufacturer's protocol.

Flow cytometric staining for CD144

48 hours post-transfection, cells were collected, washed, and resuspended in PBS + 2% FBS. Surface staining was performed with anti-CD144-APC (APC-FcA98071; clone 240755B2; Proteintech, 1:20) for 20–30 min at 4 °C in the dark. After three PBS washes, unfixed cells were analyzed by flow cytometry (APC channel; excitation ~633–640 nm, emission collected ~660 nm). Live singlets were gated; the $CD144^+$ gate was defined using an FMO control, single-stain controls were used for compensation, and the isotype control verified specificity. At least 10,000 events per sample were acquired with fixed PMT voltages, and data were analyzed in NovoExpress.

Immunofluorescence

For immunofluorescence staining of tissue sections, paraffin-embedded sections were first incubated at 70 °C for 30 minutes, followed by deparaffinization in xylene and rehydration through a graded ethanol series. After air drying, sections were rinsed three times with PBS. Antigen retrieval was performed using EDTA Antigen Retrieval Solution (P0085, Beyotime) at 95 °C for 30 min, after which the slides were allowed to cool to room temperature for 1 h. Sections were then treated with 3% hydrogen peroxide (H_2O_2) for 10 min to block endogenous peroxidase activity and subsequently incubated in blocking buffer (0.5% Triton X-100, 1% BSA, and 10% donkey serum) for 30 min at room temperature. Primary antibodies were applied and incubated overnight at 4 °C, followed by incubation with appropriate secondary antibodies. Details of the primary antibodies used are listed in Supplementary Table 3.

Distribution of clusters

To identify vascular cell clusters that are commonly shared across different studies, we computed the ratio of observed to expected (Ro/e) for each vascular cluster within each study[81]. The chi-square test was used to determine the predicted cell numbers for each combination of clusters and studies.

Functional enrichment analysis

The top 50 genes with p-values < 0.05 were selected and subjected to Gene Ontology (GO) functional annotation analysis. When fewer than 50 genes met the threshold, all available genes were used. GO enrichment analyses were performed using the clusterProfiler R package (version 4.6.2)[82].

Definition of signature gene sets

To evaluate the functional divergence among different vascular endothelial cell subclusters, we defined two functional signature gene sets: sprouting angiogenesis (http://amigo.geneontology.org/amigo/term/GO:0002040)

and leukocyte adhesion (*ICAM1*, *ICAM2*, *VCAM1*, *SELE*, *SELP*, *PECAM1*). Functional activity scores of these gene sets were calculated using the AUCell[18]. Differences were assessed using the Kruskal–Wallis test. To define and annotate endothelial cell clusters (Supplementary Fig. 3F), we utilized a reference from Travaglini et al.[83], which is available for download from the GSEA database (https://www.gsea-msigdb.org/gsea/).

Statistics and reproducibility

Cell marker genes were identified using the FindAllMarkers function in Seurat, using the Wilcoxon rank-sum test for statistical analysis and the Benjamini–Hochberg method for *p*-value correction. For comparisons of AUCell scores or $R_{M/E}$ values among multiple VECs subclusters, the Kruskal–Wallis test was used. For flow-cytometry analysis, CD144-positive cell percentages were compared using an unpaired Welch's *t* test.

Data availability

All datasets generated during this study are publicly available (Supplementary Table 1). The numerical source data are provided in Supplementary Data 1-4.

Code availability

The data analysis code used in the study is available on GitHub at https://github.com/zhao-wy-6688/ECs_athero_atlas and has been archived in Zenodo at https://doi.org/10.5281/zenodo.19233726[84].

Received: 23 April 2025; Accepted: 9 April 2026;
Published online: 17 April 2026

References

1. Guo, L., Harari, E., Virmani, R. & Finn, A. V. Linking hemorrhage, angiogenesis, macrophages, and iron metabolism in atherosclerotic vascular diseases. *Arterioscler Thromb. Vasc. Biol.* **37**, e33–e39 (2017).
2. Xu, S. et al. Endothelial dysfunction in atherosclerotic cardiovascular diseases and beyond: from mechanism to pharmacotherapies. *Pharm. Rev.* **73**, 924–967 (2021).
3. Kawabe, J. & Hasebe, N. Role of the vasa vasorum and vascular resident stem cells in atherosclerosis. *Biomed. Res. Int.* **2014**, 701571 (2014).
4. Burke-Kleinman, J. & Gotlieb, A. I. Progression of arterial vasa vasorum from regulator of arterial homeostasis to promoter of atherogenesis. *Am. J. Pathol.* **193**, 1468–1484 (2023).
5. Mosquera, J. V. et al. Integrative single-cell meta-analysis reveals disease-relevant vascular cell states and markers in human atherosclerosis. *Cell Rep.* **42**, 113380 (2023).
6. Korsunsky, I. et al. Fast, sensitive and accurate integration of single-cell data with Harmony. *Nat. Methods* **16**, 1289–1296 (2019).
7. Bashore, A. C. et al. High-dimensional single-cell multimodal landscape of human carotid atherosclerosis. *Arterioscler. Thromb. Vasc. Biol.* **44**, 930–945 (2024).
8. Alsaigh, T., Evans, D., Frankel, D. & Torkamani, A. Decoding the transcriptome of calcified atherosclerotic plaque at single-cell resolution. *Commun. Biol.* **5**, 1084 (2022).
9. Hu, Z. et al. Single-cell transcriptomic atlas of different human cardiac arteries identifies cell types associated with vascular physiology. *Arterioscler Thromb. Vasc. Biol.* **41**, 1408–1427 (2021).
10. Pan, H. et al. Single-cell genomics reveals a novel cell state during smooth muscle cell phenotypic switching and potential therapeutic targets for atherosclerosis in mouse and human. *Circulation* **142**, 2060–2075 (2020).
11. Wirka, R. C. et al. Atheroprotective roles of smooth muscle cell phenotypic modulation and the TCF21 disease gene as revealed by single-cell analysis. *Nat. Med.* **25**, 1280–1289 (2019).
12. Stuart, T. et al. Comprehensive integration of single-cell data. *Cell* **177**, 1888–1902 e1821 (2019).
13. Markova, V. et al. Endothelial cell markers are inferior to vascular smooth muscle cells markers in staining vasa vasorum and are non-specific for distinct endothelial cell lineages in clinical samples. *Int. J. Mol. Sci.* **24**, https://doi.org/10.3390/ijms24031959 (2023).
14. Xue, Z. et al. PIM1 instigates endothelial-to-mesenchymal transition to aggravate atherosclerosis. *Theranostics* **15**, 745–765 (2025).
15. Sissaoui, S. et al. Genomic characterization of endothelial enhancers reveals a multifunctional role for NR2F2 in regulation of arteriovenous gene expression. *Circ. Res.* **126**, 875–888 (2020).
16. Pan, X. et al. Tumour vasculature at single-cell resolution. *Nature* **632**, 429–436 (2024).
17. Li, J. et al. Pan-cancer integrative analyses dissect the remodeling of endothelial cells in human cancers. *Natl. Sci. Rev.* **11**, nwae231 (2024).
18. Aibar, S. et al. SCENIC: single-cell regulatory network inference and clustering. *Nat. Methods* **14**, 1083–1086 (2017).
19. Schulkens, I. A. et al. Expression, regulation and function of human metallothioneins in endothelial cells. *J. Vasc. Res.* **51**, 231–238 (2014).
20. Kudo, A. & Kii, I. Periostin function in communication with extracellular matrices. *J. Cell Commun. Signal* **12**, 301–308 (2018).
21. Morabito, S., Reese, F., Rahimzadeh, N., Miyoshi, E. & Swarup, V. hdWGCNA identifies co-expression networks in high-dimensional transcriptomics data. *Cell Rep. Methods* **3**, 100498 (2023).
22. Langer, H. F. & Chavakis, T. Leukocyte-endothelial interactions in inflammation. *J. Cell Mol. Med.* **13**, 1211–1220 (2009).
23. Libby, P. The changing landscape of atherosclerosis. *Nature* **592**, 524–533 (2021).
24. Domingues, A. et al. Targeting endothelial thioredoxin-interacting protein (TXNIP) protects from metabolic disorder-related impairment of vascular function and post-ischemic revascularisation. *Angiogenesis* **23**, 249–264 (2020).
25. Collen, D. & Lijnen, H. R. Basic and clinical aspects of fibrinolysis and thrombolysis. *Blood* **78**, 3114–3124 (1991).
26. Yang, X. et al. MicroRNA-217 ameliorates inflammatory damage of endothelial cells induced by oxidized LDL by targeting EGR1. *Mol. Cell Biochem.* **475**, 41–51 (2020).
27. Cheng, C. et al. Ets2 determines the inflammatory state of endothelial cells in advanced atherosclerotic lesions. *Circ. Res.* **109**, 382–395 (2011).
28. Camare, C., Pucelle, M., Negre-Salvayre, A. & Salvayre, R. Angiogenesis in the atherosclerotic plaque. *Redox Biol.* **12**, 18–34 (2017).
29. Adams, R. H. & Alitalo, K. Molecular regulation of angiogenesis and lymphangiogenesis. *Nat. Rev. Mol. Cell Biol.* **8**, 464–478 (2007).
30. Pepper, M. S. Transforming growth factor-beta: vasculogenesis, angiogenesis, and vessel wall integrity. *Cytokine Growth Factor Rev.* https://doi.org/10.1016/S1359-6101(96)00048-2 (1997).
31. Song, F. et al. Deletion of endothelial IGFBP5 protects against ischaemic hindlimb injury by promoting angiogenesis. *Clin. Transl. Med.* **14**, e1725 (2024).
32. Augustin, H. G., Koh, G. Y., Thurston, G. & Alitalo, K. Control of vascular morphogenesis and homeostasis through the angiopoietin-Tie system. *Nat. Rev. Mol. Cell Biol.* **10**, 165–177 (2009).
33. De Falco, S. The discovery of placenta growth factor and its biological activity. *Exp. Mol. Med.* **44**, 1–9 (2012).
34. Zhang, Y., Xu, Y., Ma, J., Pang, X. & Dong, M. Adrenomedullin promotes angiogenesis in epithelial ovarian cancer through upregulating hypoxia-inducible factor-1α and vascular endothelial growth factor. *Sci. Rep.* **7**, https://doi.org/10.1038/srep40524 (2017).
35. Kidoya, H. et al. Spatial and temporal role of the apelin/APJ system in the caliber size regulation of blood vessels during angiogenesis. *EMBO J.* **27**, 522–534 (2008).
36. Maisonpierre, P. C. et al. Angiopoietin-2, a natural antagonist for Tie2 that disrupts in vivo angiogenesis. *Science* **277**, 55–60 (1997).
37. Bornstein, P. Thrombospondins function as regulators of angiogenesis. *J. Cell Commun. Signal* **3**, 189–200 (2009).

38. Andrae, J., Gallini, R. & Betsholtz, C. Role of platelet-derived growth factors in physiology and medicine. *Genes Dev.* **22**, 1276–1312 (2008).
39. Doring, Y. et al. CXCL12 derived from endothelial cells promotes atherosclerosis to drive coronary artery disease. *Circulation* **139**, 1338–1340 (2019).
40. Zhang, M. F. et al. Catalpol attenuates ischemic stroke by promoting neurogenesis and angiogenesis via the SDF-1alpha/CXCR4 pathway. *Phytomedicine* **128**, 155362 (2024).
41. Marchand, M., Monnot, C., Muller, L. & Germain, S. Extracellular matrix scaffolding in angiogenesis and capillary homeostasis. *Semin Cell Dev. Biol.* **89**, 147–156 (2019).
42. Singh, P. et al. Inhibin is a novel paracrine factor for tumor angiogenesis and metastasis. *Cancer Res.* **78**, 2978–2989 (2018).
43. Dave, J. M. & Bayless, K. J. Vimentin as an integral regulator of cell adhesion and endothelial sprouting. *Microcirculation* **21**, 333–344 (2014).
44. Ma, Y. et al. Fascin 1 is dispensable for developmental and tumour angiogenesis. *Biol. Open* **2**, 1187–1191 (2013).
45. Roca, C. & Adams, R. H. Regulation of vascular morphogenesis by Notch signaling. *Genes Dev.* **21**, 2511–2524 (2007).
46. Atkins, G. B. & Jain, M. K. Role of Kruppel-like transcription factors in endothelial biology. *Circ. Res.* **100**, 1686–1695 (2007).
47. Nishiyama, K. et al. Id1 gene transfer confers angiogenic property on fully differentiated endothelial cells and contributes to therapeutic angiogenesis. *Circulation* **112**, 2840–2850 (2005).
48. Jiang, L. et al. Bach1 represses Wnt/beta-catenin signaling and angiogenesis. *Circ. Res.* **117**, 364–375 (2015).
49. Piera-Velazquez, S. & Jimenez, S. A. Endothelial to mesenchymal transition: role in physiology and in the pathogenesis of human diseases. *Physiol. Rev.* **99**, 1281–1324 (2019).
50. Tan, J. et al. Single-cell transcriptomics reveals crucial cell subsets and functional heterogeneity associated with carotid atherosclerosis and cerebrovascular events. *Arterioscler Thromb. Vasc. Biol.* **43**, 2312–2332 (2023).
51. Tanaka, M. et al. The endothelial adrenomedullin-RAMP2 system regulates vascular integrity and suppresses tumour metastasis. *Cardiovasc. Res.* **111**, 398–409 (2016).
52. Zhu, X. et al. Acetate controls endothelial-to-mesenchymal transition. *Cell Metab.* **35**, 1163–1178 e1110 (2023).
53. Hwang, S., Lee, D. H., Lee, I. K., Park, Y. M. & Jo, I. Far-infrared radiation inhibits proliferation, migration, and angiogenesis of human umbilical vein endothelial cells by suppressing secretory clusterin levels. *Cancer Lett.* **346**, 74–83 (2014).
54. Danziger, J. Vitamin K-dependent proteins, warfarin, and vascular calcification. *Clin. J. Am. Soc. Nephrol.* **3**, 1504–1510 (2008).
55. Chen, Y. et al. Omentin-1 is associated with atrial fibrillation in patients with cardiac valve disease. *BMC Cardiovasc. Disord.* **20**, 214 (2020).
56. Sharifi, M. A. et al. ADAMTS-7 modulates atherosclerotic plaque formation by degradation of TIMP-1. *Circ. Res.* **133**, 674–686 (2023).
57. Ma, Q. et al. SRGN, a new identified shear-stress-responsive gene in endothelial cells. *Mol. Cell Biochem.* **474**, 15–26 (2020).
58. Deheuninck, J. & Luo, K. Ski and SnoN, potent negative regulators of TGF-beta signaling. *Cell Res.* **19**, 47–57 (2009).
59. Dabravolski, S. A. et al. The role of KLF2 in the regulation of atherosclerosis development and potential use of KLF2-targeted therapy. *Biomedicines* **10**, https://doi.org/10.3390/biomedicines10020254 (2022).
60. Matrone, G. et al. Lmo2 (LIM-domain-only 2) modulates Sphk1 (Sphingosine Kinase) and promotes endothelial cell migration. *Arterioscler Thromb. Vasc. Biol.* **37**, 1860–1868 (2017).
61. Harris, E. S. & Nelson, W. J. VE-cadherin: at the front, center, and sides of endothelial cell organization and function. *Curr. Opin. Cell Biol.* **22**, 651–658 (2010).
62. Traeuble, K. et al. Integrated single-cell atlas of human atherosclerotic plaques. *Nat. Commun.* **16**, 8255 (2025).
63. Bleckwehl, T. et al. Encompassing view of spatial and single-cell RNA sequencing renews the role of the microvasculature in human atherosclerosis. *Nat. Cardiovasc. Res.* **4**, 26–44 (2025).
64. Rood, J. E., Maartens, A., Hupalowska, A., Teichmann, S. A. & Regev, A. Impact of the Human Cell Atlas on medicine. *Nat. Med.* **28**, 2486–2496 (2022).
65. Dhanasekaran, R. et al. Activation of the transforming growth factor-beta/SMAD transcriptional pathway underlies a novel tumor-promoting role of sulfatase 1 in hepatocellular carcinoma. *Hepatology* **61**, 1269–1283 (2015).
66. Glaser, S. F. et al. The histone demethylase JMJD2B regulates endothelial-to-mesenchymal transition. *Proc. Natl. Acad. Sci. USA* **117**, 4180–4187 (2020).
67. Wang, S. et al. QSulf1, a heparan sulfate 6-O-endosulfatase, inhibits fibroblast growth factor signaling in mesoderm induction and angiogenesis. *Proc. Natl. Acad. Sci. USA* **101**, 4833–4838 (2004).
68. Hao, Y. et al. Integrated analysis of multimodal single-cell data. *Cell* **184**, 3573–3587.e3529 (2021).
69. Germain, P. L., Lun, A., Garcia Meixide, C., Macnair, W. & Robinson, M. D. Doublet identification in single-cell sequencing data using scDblFinder. *F1000Res.* **10**, 979 (2021).
70. Yang, S. et al. Decontamination of ambient RNA in single-cell RNA-seq with DecontX. *Genome Biol.* **21**, 57 (2020).
71. Alquicira-Hernandez, J. & Powell, J. E. Nebulosa recovers single-cell gene expression signals by kernel density estimation. *Bioinformatics* **37**, 2485–2487 (2021).
72. Virshup, I. et al. The scverse project provides a computational ecosystem for single-cell omics data analysis. *Nat. Biotechnol.* **41**, 604–606 (2023).
73. Gayoso, A. et al. A Python library for probabilistic analysis of single-cell omics data. *Nat. Biotechnol.* **40**, 163–166 (2022).
74. Badia, I. M. P. et al. decoupleR: ensemble of computational methods to infer biological activities from omics data. *Bioinform Adv.* **2**, vbac016 (2022).
75. Adelus, M. L. et al. Single-cell 'omic profiles of human aortic endothelial cells in vitro and human atherosclerotic lesions ex vivo reveal heterogeneity of endothelial subtype and response to activating perturbations. *Elife* **12**, https://doi.org/10.7554/eLife.91729 (2024).
76. Hall, I. F., Kishta, F., Xu, Y., Baker, A. H. & Kovacic, J. C. Endothelial to mesenchymal transition: at the axis of cardiovascular health and disease. *Cardiovasc. Res.* **120**, 223–236 (2024).
77. Chen, P. Y. et al. Endothelial-to-mesenchymal transition drives atherosclerosis progression. *J. Clin. Invest.* **125**, 4514–4528 (2015).
78. Yori, J. L., Johnson, E., Zhou, G., Jain, M. K. & Keri, R. A. Kruppel-like factor 4 inhibits epithelial-to-mesenchymal transition through regulation of E-cadherin gene expression. *J. Biol. Chem.* **285**, 16854–16863 (2010).
79. Moonen, J. R. et al. Endothelial progenitor cells give rise to pro-angiogenic smooth muscle-like progeny. *Cardiovasc. Res.* **86**, 506–515 (2010).
80. Kanisicak, O. et al. Genetic lineage tracing defines myofibroblast origin and function in the injured heart. *Nat. Commun.* **7**, 12260 (2016).
81. Zhang, L. et al. Lineage tracking reveals dynamic relationships of T cells in colorectal cancer. *Nature* **564**, 268–272 (2018).
82. Xu, S. et al. Using clusterProfiler to characterize multiomics data. *Nat. Protoc.* **19**, 3292–3320 (2024).
83. Travaglini, K. J. et al. A molecular cell atlas of the human lung from single-cell RNA sequencing. *Nature* **587**, 619–625 (2020).
84. Wu, Y. ECs_athero_atlas. *Zenodo*, https://doi.org/10.5281/zenodo.19233726 (2026).
85. Fu, M. et al. Single-cell RNA sequencing of coronary perivascular adipose tissue from end-stage heart failure patients identifies

SPP1(+) macrophage subpopulation as a target for alleviating fibrosis. *Arterioscler. Thromb. Vasc. Biol.* **43**, 2143–2164 (2023).
86. Gole, S., Tkachenko, S., Masannat, T., Baylis, R. A. & Cherepanova, O. A. Endothelial-to-mesenchymal transition in atherosclerosis: friend or foe? *Cells* **11**, https://doi.org/10.3390/cells11192946 (2022).
87. Depuydt, M. A. C. et al. Microanatomy of the human atherosclerotic plaque by single-cell transcriptomics. *Circ. Res.* **127**, 1437–1455 (2020).

Acknowledgements

GEO and Zenodo databases provided the analyzed datasets. Graphical abstract was created in BioRender (Wu, Y., 2026; https://BioRender.com/8f5wwh2). We thank the Department of Cardiology, Qilu Hospital of Shandong University, Jinan, Shandong, 250012, China, for providing HUVECs. This work was supported by the Department of Science & Technology of Shandong Province (ZR2023MH023), the Shandong Province Key Research and Development Program (2024CXGC010606), the Clinical Research Project of Shandong University (2021SDUCRCA009), and the National Health Commission Capacity Building and Continuing Education Center Nervous system and minimally invasive intervention project fund (1003).

Author contributions

Y.W., Z.X., T.S., L.C., A.T. and D.W. designed this study and wrote the paper; Z.X. performed the experiments; Y.W., Z.X., T.S. and Y.Y. analyzed the data; X.L., W.X., F.M., Z.Z., M.L., L.L. and M.H. contributed to sample processing and technical validation. All authors read and approved the final version of the manuscript.

Competing interests

The authors declare no competing interests.

Additional information

Supplementary information The online version contains supplementary material available at https://doi.org/10.1038/s42003-026-10095-1.

Correspondence and requests for materials should be addressed to Lian Cheng, Anton Gisterå or Donghai Wang.

Peer review information *Communications Biology* thanks Floriana Maria Farina and the other, anonymous, reviewers for their contribution to the peer review of this work. Primary Handling Editors: Kaoru Ito and Dario Ummarino. A peer review file is available.